

Multimodal Fusion Network for Micro-displacement Measurement via Michelson Interferometer

ZIXING JIA,^{1,*} JIAWEI LI,¹ ZIPING CHEN¹, XIN LI¹

¹*School of Physics and Astronomy, Sun Yat-Sen University, Zhuhai 519082, China*

**jjazx5@mail2.sysu.edu.cn*

Abstract: We propose a multimodal fusion network (MFN) for precise micro-displacement measurement using a modified Michelson interferometer. The model resolves the intrinsic $\lambda/2$ phase ambiguity that limits conventional single-wavelength interferometry by introducing a dual-head learning mechanism: one head performs sub- $\lambda/2$ displacement regression, and the other classifies integer interference orders. Unlike dual-wavelength or iterative fitting methods, which require high signal quality and long computation time, MFN achieves robust, real-time prediction directly from interferometric images.

Trained on 2×10^5 simulated interferograms and fine-tuned with only $\sim 0.24\%$ of real experimental data (about 500 images), the model attains a displacement precision of 4.84 ± 0.15 nm and an order-classification accuracy of 98%. Even under severe noise, MFN maintains stable accuracy (about 16 nm RMSE), whereas conventional heuristic algorithms exhibit errors exceeding 100 nm. These results demonstrate that MFN offers a fast, noise-tolerant, and cost-efficient solution for single-wavelength interferometric metrology, eliminating the need for multi-wavelength hardware or complex phase fitting.

1. Introduction

Michelson interferometer, since its invention in the late 19th century, has become one of the most fundamental instruments in modern precision metrology owing to its high sensitivity, simple structure, and easily controllable optical path. It plays an indispensable role in various fields such as gravitational-wave detection [1, 2], precision metrology [3] and materials science [4]. However, the traditional Michelson interferometer architecture also exhibits inherent limitations. When the measured displacement exceeds half of the light wavelength (i.e., beyond $\lambda/2$), the interference signal suffers from a 2π phase ambiguity. Consequently, the displacement information obtained from the interference fringes or fitting equations becomes non-unique, leading to periodic errors or discontinuous phase jumps in the measurement results. To overcome this problem, several improved techniques have been developed, including dual-wavelength interferometry [5–7], and wavelength scanning interferometry [8–10].

Neural networks can learn nonlinear mappings directly from data [11], capturing both spatial and temporal dependencies without relying on specific fitting formulas. This property is particularly beneficial for interferometric imaging, where signal degradation due to speckle, vibration, or defocus can severely hinder analytical reconstruction. Moreover, once trained, a neural network offers extremely fast inference [12], allowing real-time or high-throughput displacement evaluation

Recent years have witnessed a rapid proliferation of deep learning methods in optical and photonic measurement fields. Notably, the extraction of phase information from interference fringes has seen significant advances in recent years. Deep learning-based fringe projection profilometry (FPP) [13–15] methods now reconstruct the three-dimensional (3D) shape of target objects by extracting phase information from interference patterns. This method outperforms traditional phase-shifting techniques—such as three-step phase-shifting (PS) and Fourier transform methods—in both processing speed and noise robustness.

This trend motivates us to explore its application in Michelson interferometry for displacement measurement. In practical scenarios, interference fringes are inevitably contaminated by displacement-dependent noise—for example, information related to object tilting. Compared to Least squares fitting approaches, our proposed deep learning-based scheme requires minimal additional hardware yet overcomes inherent displacement limitations. Furthermore, when applied to real-world images with strong noise, it achieves superior performance over standard fitting algorithms—such as differential evolution (DE) [16] and quasi-Newton methods—in both computational efficiency and noise resilience.

We develop a multimodal fusion network (MFN) that integrates spatial, spectral, and temporal cues [17] from interferometric sequences to achieve robust and precise micro-displacement prediction. The proposed model jointly processes raw interferograms, their differential and frequency-domain representations, together with statistical temporal descriptors, through a unified data-driven framework. In contrast to previous fitting-based approaches, our method bypasses explicit phase unwrapping and directly regresses displacement magnitude with high precision and stability. Experimental results on data acquired from a modified Michelson interferometer demonstrate that the MFN remains robust and short fitting duration across diverse noise levels, representing a significant advancement toward practical, learning-based interferometric metrology.

2. Methods

2.1. Overview of Michelson Interferometry Principle

According to the basic principle of Michelson interference [18], the intensity of the interference fringes is:

$$I(x, y) = \tilde{I}_0(1 + V \cos \delta(x, y)) \quad (1)$$

where \tilde{I}_0 is the sum of the intensities of the two beams and V is a constant with values ranging from 0 to 1. The information about the optical path difference is hidden in the phase δ . Considering the symmetry of the interference fringes, we can expand the dipole term of δ :

$$\delta(x, y) = \phi + ar^2 + br^4 \quad (2)$$

with the radius

$$r^2 = (x - x_0)^2 + (y - y_0)^2 \quad (3)$$

where x_0 and y_0 are the positions of the centers of the interference fringes and a, b represent the coefficients. ϕ is the phase corresponding to the center of the stripe, including the interference order ($\phi = 2\pi m$).

Since the laser used is a Gaussian beam ($\tilde{I}_0 = I_0 e^{d[(x-x_c)^2 + (y-y_c)^2]}$, x_c and y_c are the coordinates of the point with the highest light intensity). Therefore, the final light intensity formula is (Model with background noise added):

$$I(x, y) = I_0 e^{d[(x-x_c)^2 + (y-y_c)^2]} (1 + V \cos(2\pi m + ar^2 + br^4)) + k \quad (4)$$

To enhance robustness and convergence, the parameter estimation is performed via a two-stage optimization strategy, which we term the Heuristic Analytical algorithm (HAA):

1. **Global search:** A differential evolution (DE) algorithm is used for robust global optimization over the parameter space. The initial population is generated using a Sobol [19] low-discrepancy sequence to ensure uniform coverage and avoid premature convergence.
2. **Local refinement:** The best solution from DE is refined using gradient-based optimizers (L-BFGS-B [20], TNC [21], or SLSQP [22]) to achieve high-precision convergence.

Prior to fitting, each image undergoes preprocessing:

- Images are downsampled to 75% of their original size using bilinear interpolation to accelerate computation.
- A small Gaussian blur ($\sigma = 0.5$ pixels) is applied to suppress high-frequency noise.
- Pixel intensities are normalized to the range $[0, 1]$.

m is used to compute displacement. According to the principle of Michelson interferometry, the change in displacement ΔL between consecutive frames relates to the phase change Δm by

$$\Delta L = \Delta m \frac{\lambda}{2} \quad (5)$$

However, it is worth noting that the above fitting can only yield the fractional part of m . Only under limited precision—specifically, when the change in m between consecutive frames is small—can a sudden drop in an otherwise increasing m sequence (or a sudden rise in an otherwise decreasing sequence) be corrected by manually adding 1 (or subtracting 1) to the subsequent m values. To mitigate the effects of noise, the current method employs a rule: if an anomalous jump in $|\Delta m|$ exceeds 0.3, the integer order is corrected by ± 1 .

2.2. Model Architecture Overview

We propose a multimodal fusion network that integrates both image-based and temporal statistical cues to predict nanoscale displacements with explicit order awareness. As illustrated in Figure 1, the overall framework retains a three-branch fusion design consisting of two image-based feature extraction pathways and one numerical modeling branch. On top of these, two parallel prediction heads are introduced: one for continuous displacement regression and another for discrete order classification. This design allows the model to disentangle fine-grained sub-period estimation from integer-order ambiguity inherent to interferometric measurements.

The first image branch comprises three parallel single-channel convolutional subnetworks, each processing a distinct visual modality: the raw interferogram (encoding spatial phase structures), the frame-difference image (capturing dynamic motion patterns), and the FFT-domain representation (reflecting global frequency distributions) [23, 24]. Each subnetwork produces a 128-dimensional feature vector that preserves modality-specific information without mutual interference. The second image branch employs a MobileViT [25] backbone that fuses the three modalities as a joint three-channel input. Through transformer-based self-attention, it models long-range spatial dependencies and cross-channel interactions, providing global contextual cues complementary to local CNN representations [26].

The third branch encodes a short temporal sequence of seven scalar descriptors (e.g., image entropy, fringe contrast, intensity variance) using a Long Short-Term Memory (LSTM) network [27]. This branch is activated only during the fine-tuning stage and is specifically designed to capture the statistical relationship between noise evolution and interference order transitions. In essence, it functions as a dedicated module that learns the complex mapping from noise patterns and temporal cues to discrete order categories within the interferometric system.

The outputs of all branches are concatenated into a 640-dimensional multimodal feature vector. From this joint representation, two prediction heads are constructed independently. The *displacement head* receives features from the two image-based branches and performs regression over the continuous range $[0, \lambda/2]$, corresponding to the fractional optical path difference within one half-wavelength. The *order head*, in contrast, receives the full concatenated representation (including the LSTM embedding) and classifies the interference order into one of five categories $\{-2, -1, 0, 1, 2\}$. These two heads are trained jointly but maintain separate fully connected layers from the feature concatenation stage onward, avoiding feature entanglement [28] that might

otherwise arise from a shared latent representation. A soft orthogonality constraint [29, 30] between their final hidden representations further enforces statistical independence, preventing either branch from learning redundant or noise-correlated cues.

This modular design allows the network to simultaneously model continuous and discrete components of displacement, achieving robust performance across varying levels of interferometric noise and optical degradation.

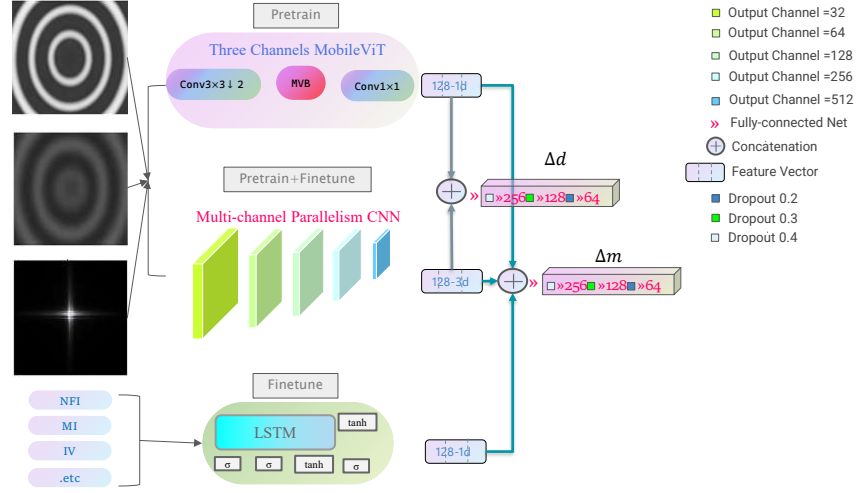


Fig. 1. Architecture of the proposed multimodal fusion network. The model integrates: (1) three single-channel CNNs for raw, differential, and FFT-transformed interferograms (local features); (2) a MobileViT backbone for joint global feature extraction; and (3) an LSTM encoder for temporal numerical descriptors (activated only during fine-tuning). The multimodal feature vector branches into two parallel heads: a displacement regression head that utilizes features from the two image-based branches (CNN + MobileViT) to achieve high-precision prediction of sub- $\lambda/2$ displacements, and an order classification head that combines features from all three branches (CNN + MobileViT + LSTM) to learn the complex mapping from images and noise statistics to interference orders. Both heads are regularized by an orthogonality loss to ensure feature disentanglement.

2.3. Feature Representation and Temporal-Spatial Encoding

To enable displacement prediction from interferometric image sequences, we preprocess each frame into three image channels and one 7-dimensional numerical feature vector. This multimodal design enriches the learning representation and injects both spatial and statistical cues into the regression model [31]. The three image channels and the seven numerical descriptors are summarized in Table 1.

To accommodate the hybrid nature of our network—where the numerical branch processes time-series sequences while the image branches operate on single-frame inputs—we implement a sliding-window strategy during data preparation. For each target frame I_t , the image-branch inputs are produced from the single frame I_t (yielding I_{orig} , I_{diff} and I_{fft}), while the numerical branch consumes a short temporal sequence of the scalar descriptors to capture temporal evolution.

Concretely, the numerical branch receives a window of 7-dimensional feature vectors

$$\{\mathbf{f}_{t-\tau}, \dots, \mathbf{f}_t\}, \quad \mathbf{f}_s \in \mathbb{R}^7, \quad (6)$$

Category	Feature Name	Formula
Image Channels	Original Interferogram	$I_{\text{orig}}(x, y) = I_t(x, y)$
	Frame Difference Image	$I_{\text{diff}}(x, y) = I_t(x, y) - I_{t-1}(x, y) $
	Frequency-Domain Image	$I_{\text{fit}}(u, v) = \frac{\log(\mathcal{F}[I_t](u, v) + \epsilon) - \min}{\max - \min}$
Numerical Channels	Normalized Frame Index	$f_1 = \frac{t}{T-1}$
	Mean Intensity	$f_2 = \frac{1}{HW} \sum_{x=1}^H \sum_{y=1}^W I_t(x, y)$
	Intensity Variance	$f_3 = \frac{1}{HW} \sum_{x,y} (I_t(x, y) - f_2)^2$
	Number of Horizontal Fringe Peaks	$f_4 = \text{PeakCount}(P(y)), \quad P(y) = \frac{1}{H} \sum_{x=1}^H I_t(x, y)$
	Low-Frequency Energy Ratio	$f_5 = \frac{\sum_{(u,v) \in M} \hat{I}(u, v) ^2}{\sum_{(u,v)} \hat{I}(u, v) ^2}$
	Spectral Centroid Distance	$f_6 = \sqrt{(\bar{u} - u_0)^2 + (\bar{v} - v_0)^2}, \quad \bar{u} = \frac{\sum_u u \cdot \sum_v \hat{I}(u, v)}{\sum_{u,v} \hat{I}(u, v)}$
Image Entropy	$f_7 = -\sum_{i=1}^{256} p_i \log_2(p_i + \delta)$	

Table 1. Feature representation and temporal–spatial encoding. Key symbols: $I_t(x, y)$ = interferometric frame at time t ; H, W = image dimensions; T = total frames; \mathcal{F} = 2D FFT; ϵ, δ = small constants; M = low-frequency mask, (u_0, v_0) = frequency center; p_i = histogram bin. For the meaning of each feature’s specific formula and the reasons why we chose this feature, please refer to the supplementary materials.

where the window length is $L_w = \tau + 1$. In our experiments we choose $L_w \in [2, 5]$ (i.e., $\tau \in [1, 4]$), which balances the need to capture short-term dynamics against computational cost and model stability. Shorter windows (e.g., near sequence starts) are zero-padded to match the batch maximum window length L_{max} during collating. The collate function therefore emits:

$$\text{numerical_seq_batch} \in \mathbb{R}^{N \times L_{\text{max}} \times 7}, \quad \text{seq_lengths} \in \mathbb{N}^N, \quad (7)$$

where N is the minibatch size. Here $\text{seq_lengths} = [\ell_1, \dots, \ell_N]$ is an integer vector with each ℓ_n indicating the true (unpadded) length of the n -th sequence in the batch; by construction $1 \leq \ell_n \leq L_{\text{max}}$.

In the model forward pass the numerical batch and seq_lengths are used together so the LSTM can correctly ignore padding. In practice we employ one of the following standard strategies:

- **Packed sequences:** use PyTorch’s `pack_padded_sequence` before feeding the LSTM and `pad_packed_sequence` after, which requires sequences to be sorted by decreasing length.

- **Masking:** process the padded tensor directly and apply an explicit mask derived from `seq_lengths` when computing LSTM outputs / losses, thus zeroing contributions from padded time steps.

Both approaches prevent gradients and statistics from being contaminated by padding values and allow the LSTM to focus on real temporal information. After encoding, the numerical branch yields a fixed-dimensional embedding (e.g., by taking the last valid hidden state or via an attention/pooling over time), which is then concatenated with the image-branch embeddings to form the joint representation for regression.

This sliding-window design therefore captures short-term temporal dynamics in the numerical domain while keeping the image-branch computation frame-level and efficient. The combined representation benefits from both spatial detail (via per-frame CNN/MobileViT features) and temporal context (via the LSTM over numerical statistics), improving robustness when interferogram quality varies across frames.

2.4. Training and optimization

The network is trained in two stages. In the first stage, a large corpus of simulated interferometric data is used to pretrain the displacement regression branch. The simulated data cover random phase shifts, varying contrast, and additive noise, enabling the model to learn the nonlinear mapping between interferogram structure and fractional displacement within $[0, \lambda/2]$. During this pretraining phase, only the CNN and MobileViT branches are active; the LSTM and order-classification head remain uninitialized. The objective function is the mean squared error between predicted and ground-truth displacement:

$$L_{\text{pre}} = \frac{1}{N} \sum_{i=1}^N (\hat{d}_i - d_i)^2. \quad (8)$$

In the second stage, the model is fine-tuned on real interferometric sequences collected from the experimental setup. During this phase, the MobileViT backbone and the first three convolutional layers in each CNN branch are frozen to preserve the spatial priors obtained during pretraining, while the LSTM branch and both output heads are optimized simultaneously. The loss function plays a crucial role in determining the quality and stability of image-based learning [32]; therefore, two independent objective functions are formulated for the displacement regression head and the order classification head.

For the displacement branch, the optimization objective is defined as:

$$L_{\text{Displacement}} = \alpha L_{\text{disp}} + \gamma L_{\text{orth}}, \quad (9)$$

where

$$L_{\text{disp}} = \frac{1}{N} \sum_{i=1}^N (\hat{d}_i - d_i)^2, \quad (10)$$

and $L_{\text{orth}} = \|h_s^\top h_n\|^2$ represents the orthogonality constraint between the final hidden representations h_s (displacement head) and h_n (order head). This orthogonality regularization discourages redundant correlations between the two prediction subspaces, promoting the separation of continuous and categorical information.

Similarly, the order classification branch is optimized using:

$$L_{\text{Order}} = \beta L_{\text{order}} + \gamma L_{\text{orth}}, \quad (11)$$

where

$$L_{\text{order}} = -\frac{1}{N} \sum_{i=1}^N \sum_k y_{i,k} \log(\hat{p}_{i,k}), \quad (12)$$

is the standard cross-entropy loss over the discrete order classes $\{-2, -1, 0, 1, 2\}$. The shared orthogonality term in both equations ensures consistent feature decoupling during joint optimization.

All experiments employ the Adam optimizer [33] with a learning rate of 1×10^{-4} and weight decay of 5×10^{-5} . The coefficients α , β , and γ are selected empirically to achieve a stable balance between regression precision, classification accuracy, and feature independence, typically (1.0, 0.5, 0.05).

This fine-tuning strategy enables the network to leverage the pretrained displacement mapping while simultaneously learning to infer the discrete interference order from temporal and noise-related cues.

3. Experiments

3.1. Optical Interferometer Experiment

Because our task is a supervised learning problem, it is necessary to obtain paired data consisting of samples and corresponding ground-truth labels. The purpose of this experiment is to generate large-scale interferometric fringe images and their associated displacement data for model training and validation.

As illustrated in Fig. 2, we developed a fully automated data acquisition system based on a modified Michelson interferometer [34]. The system mainly includes an interferometer (*SGM-4 / Shanghai Sino-Guangming Co., Ltd.*), a camera (*Daheng MER-130-30UM*), and a voltage-controlled piezoelectric actuator (*PST150/2×3/10 / XinTian Tech.*). By varying the driving voltage of the actuator, the relative displacement between the two interferometer arms changes, producing different interference patterns. During this process, both voltage and image data are recorded automatically and synchronously, forming a dataset that directly links interferograms to displacement values.

To eliminate human-introduced errors during measurement, the acquisition is fully automated [35] through a custom control program, ensuring stable and repeatable measurements. To reduce environmental interference such as airflow and vibration, the optical path is enclosed with acrylic panels, effectively improving the stability and consistency of the captured interferograms.

Detailed specifications of all optical and electronic components are provided in the Supplement Document.

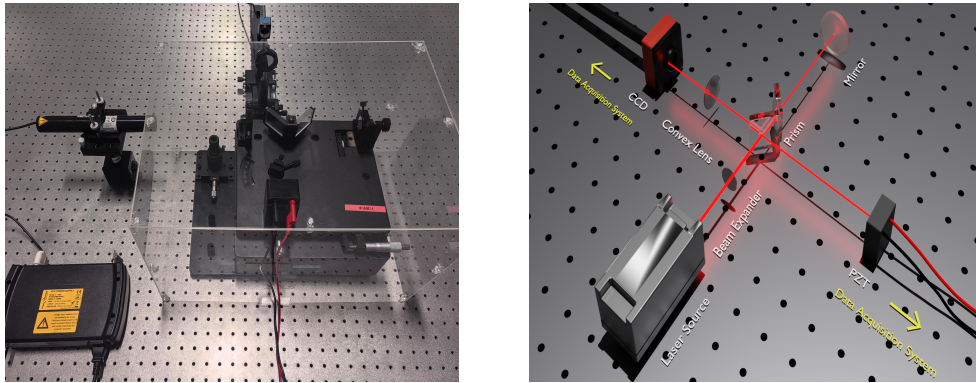


Fig. 2. **(Left)** Photograph of the modified Michelson interferometer setup. **(Right)** Schematic of the modified Michelson interferometer. Key components include: a He-Ne laser, beam expander and collimator, convex lens, prism-based beam splitter, movable mirror mounted on a piezoelectric actuator, fixed mirror, and CCD camera. Red lines indicate the optical path

3.2. Voltage–Displacement Characterization of the Piezoelectric Actuator

To obtain the labels required for supervised training, it is necessary to calibrate the voltage–displacement (V – d) relationship of the piezoelectric actuator. As shown in Fig. 3, this measurement is performed using a capacitive micrometer (specific model provided in the Supplement Document).

Considering that the piezoelectric actuator exhibits hysteresis and other nonlinear effects, it is essential to accurately measure its actual displacement response to the applied voltage. To achieve this, we developed an automated measurement system similar to the interferometric acquisition setup described in the previous section. This system controls the applied voltage to the actuator and synchronously records both voltage and displacement data from the capacitive micrometer.

To ensure consistency between the interferometric dataset and the displacement calibration, the amplitude of voltage variation and the dwell time at each voltage level are kept identical to those used in the interferometer experiment. This guarantees that the previously obtained image–voltage pairs can be reliably converted into image–displacement pairs through the measured V – d relationship.

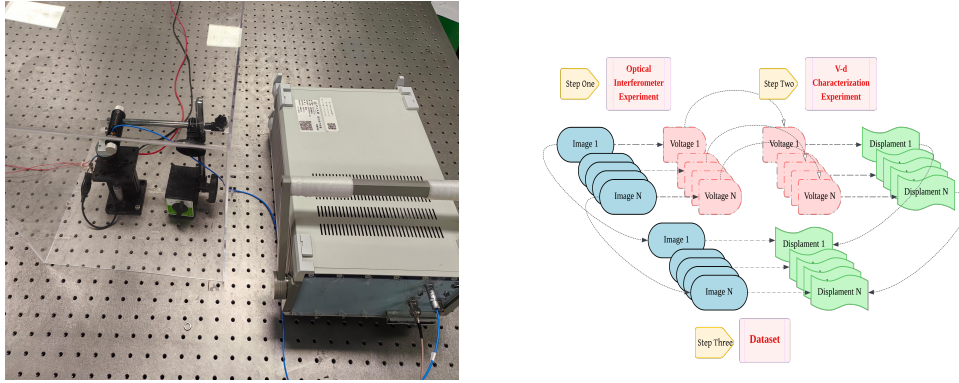


Fig. 3. **(Left)** Photograph of the voltage–displacement (V – d) characterization setup, showing the piezoelectric actuator mounted on the capacitive micrometer inside an acrylic enclosure. **(Right)** A brief description of the two experimental objectives: The first experimental goal is to obtain images aligned with voltage, and the second experiment is to obtain images aligned with displacement, ultimately resulting in the dataset we need, which is images and displacement.

4. Results and Discussion

4.1. Performance under Different Noise Conditions

Excluding the LSTM branch, which serves as the noise-related encoder during fine-tuning, the remaining image-based components of the network contain approximately eight million trainable parameters. To ensure stable convergence and physically meaningful representation learning, we generated about 2×10^5 simulated interferograms as the training and validation sets for pretraining. Each simulated image was embedded with mild Gaussian noise and fringe-contrast variation to align with the distribution of real measurements (details of the simulation procedure are provided in the Supplementary Materials). After pretraining, the model achieved a validation displacement accuracy of approximately 4.84 ± 0.15 nm (the assessment methods are described in the Supplementary Materials), demonstrating that the regression branch successfully captured the sub-wavelength mapping from interferometric features to micro-displacements.

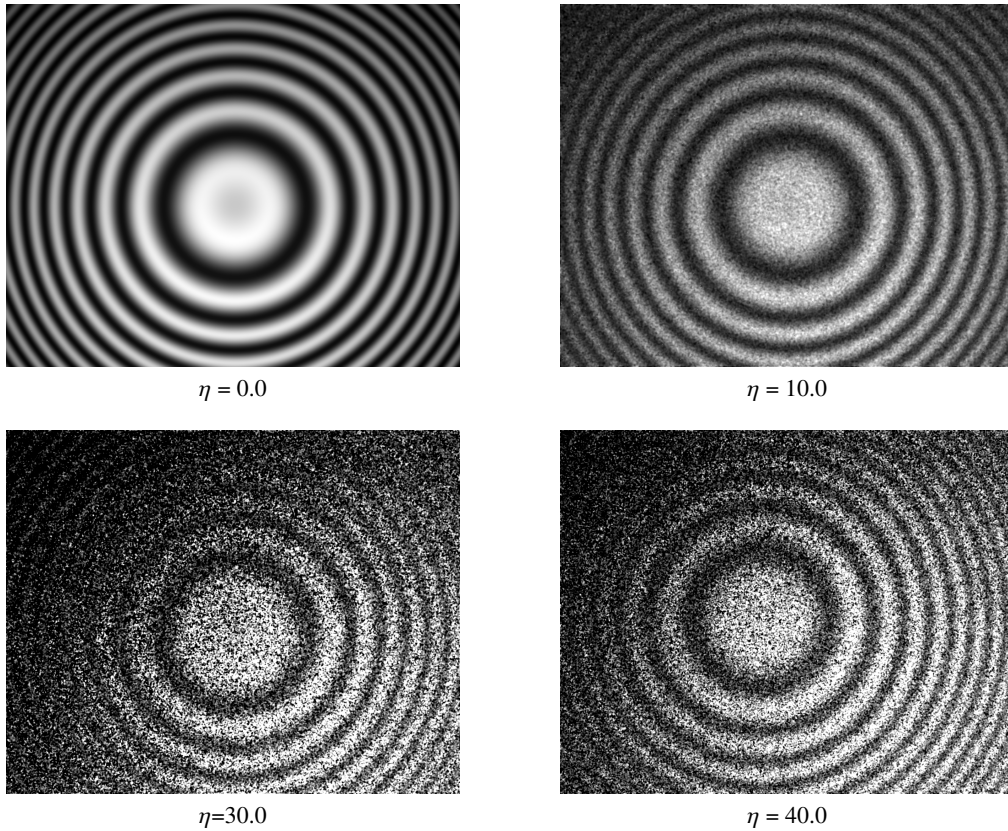


Fig. 4. The image demonstrates different eta values. In the experiment, the range was obtained using the original fitting formula, based on three times the standard deviation of parameters derived from the actual image(I). Subsequently, simulated images were generated through randomization, incorporating noise sources such as laser power drift, photon Poisson noise, CCD readout Gaussian noise, the optical system's inherent PSF, salt-and-pepper noise, and background gradients caused by uneven illumination. The total illumination was calculated as I' and η controls the overall noise intensity. After η control, the final luminance output is $I_{final} = I + \eta \times (I' - I)$

To further investigate the robustness and inference efficiency of the proposed MFN, we comprehensively modeled multiple realistic noise sources, including Gaussian noise, Poisson noise, fringe-intensity center drift, and random phase perturbations. A unified noise intensity parameter, denoted as η , was introduced to control the overall level of image degradation (examples of interferograms under different η values are shown in Fig. 4). We selected nine discrete noise intensities uniformly distributed over the range $\eta \in [0, 40]$ to quantitatively evaluate the anti-noise capability and inference speed of MFN, and to compare its performance with that of the traditional Heuristic Analytical Algorithm (HAA).

As illustrated in Fig. 5, while the HAA achieves sub-nanometer fitting accuracy at low noise levels, its performance rapidly deteriorates as η increases—exceeding 100 nm RMSE when $\eta = 40$, primarily due to unstable phase-fitting under high noise contamination. In contrast, the MFN maintains stable regression accuracy across all noise intensities, with an average prediction error of about 16 nm even at the highest η . Regarding inference efficiency, the MFN requires only a single forward pass per image, whereas the HAA depends on iterative heuristic optimization. Consequently, the MFN achieves over four orders of magnitude speedup in per-frame processing, demonstrating its suitability for high-throughput or real-time interferometric applications.

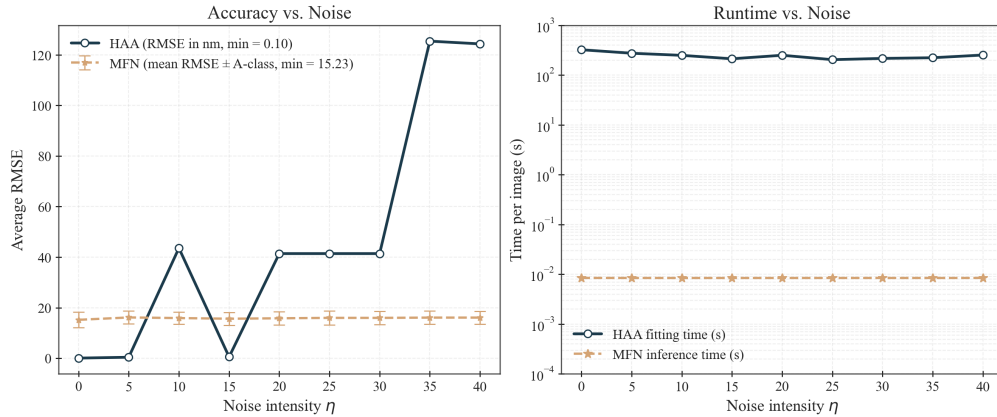


Fig. 5. **Left:** Average displacement prediction accuracy (RMSE in nanometers) versus noise intensity. Due to the high computational cost of the HAA, its performance was evaluated on sampled interferogram subsets for each noise level. In contrast, the MFN was evaluated on all available sequences at every η , enabling the estimation of Type-A uncertainties shown as error bars. **Right:** Inference time per image versus noise intensity. The MFN model was trained and tested on an NVIDIA L40 GPU. For the HAA, the iterative optimization process was capped at a maximum runtime of 10^3 s per image to prevent unbounded fitting time; without this restriction, convergence failures frequently occurred at high noise intensities, with runtimes exceeding 10^4 s and no valid solution found. The results highlight that the MFN maintains stable precision and achieves over four orders of magnitude acceleration compared with the traditional HAA, even under severe noise degradation.

4.2. Effect of Fine-tuning Data Volume on Classification Performance

In practical deployment, the amount of real data available for fine-tuning can vary significantly depending on experimental conditions and acquisition cost. In this section, we focus on the performance of the *order classification head*, which is responsible for predicting the discrete interference order. This task provides a more direct indicator of the model’s domain adaptation capability than absolute displacement regression, since accurate order recognition reflects

the network’s ability to capture essential interference semantics under real noise and contrast variations. Therefore, the classification accuracy serves as the primary metric for assessing fine-tuning effectiveness across different dataset sizes.

To quantitatively evaluate how data volume affects convergence behavior and final performance, we fine-tuned the pretrained model using subsets of different sizes drawn from the real interferometric dataset. The horizontal axis in Fig. 6 denotes the number of fine-tuning images, and both validation and test accuracies were measured on a fixed test set containing 2.5×10^3 images. All experiments were performed under identical hardware and hyperparameter settings, and each fine-tuning process completed within 10–15 minutes.

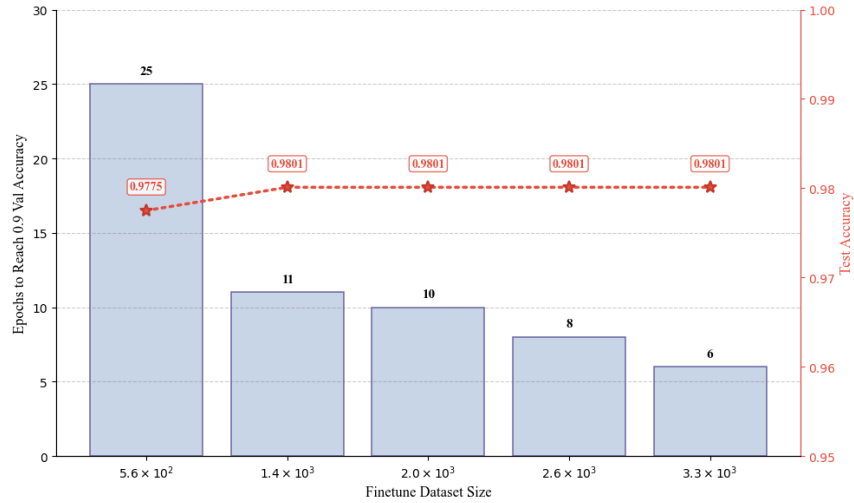


Fig. 6. Influence of fine-tuning dataset size on the convergence speed and classification accuracy of the order prediction head. The horizontal axis represents the number of fine-tuning images, and the left vertical axis (blue bars) indicates the number of epochs required to reach 0.9 validation accuracy. The red curve (right axis) shows the final test accuracy on a fixed test set of 2.5×10^3 images. All experiments were conducted on the same hardware platform, and each fine-tuning process completed within 10–15 minutes.

As shown in Fig. 6, the model achieves 0.9 validation accuracy within fewer than 30 epochs once the fine-tuning dataset size exceeds approximately 5×10^2 images, corresponding to about 0.24% of the pretraining dataset. When the data size increases further, the number of epochs required for convergence drops rapidly—from 25 to fewer than 6, while the test accuracy stabilizes around 98%. This demonstrates that even a small number of real interferograms are sufficient to adapt the classification head to real experimental conditions, significantly reducing the calibration cost and data acquisition burden. Such results also indicate that the high-level decision boundaries learned from simulated data generalize effectively to real-world interferometric patterns, validating the robustness and transferability of the proposed multimodal architecture.

From an application perspective, this data efficiency is particularly advantageous in industrial or laboratory setups where collecting large volumes of labeled interferograms is impractical. The ability to achieve near-saturated accuracy with only a few hundred samples highlights the practicality of the MFN framework for rapid deployment and online adaptation across diverse optical systems.

5. Conclusion

In this work, we proposed a multimodal fusion network (MFN) to address the intrinsic $\lambda/2$ phase ambiguity that constrains single-wavelength interferometric displacement measurement. By integrating image-based features and temporal statistical cues within a dual-head architecture, the model performs sub- $\lambda/2$ displacement regression and integer-order classification simultaneously, yielding a unified and physically interpretable displacement estimation framework. Unlike traditional dual-wavelength approaches that require high signal quality and complex optical setups, MFN resolves the $\lambda/2$ ambiguity purely through learning-based inference, maintaining accuracy and stability even under strong noise or fringe degradation. This data-driven strategy enables precise displacement prediction using a single optical channel, reducing both hardware complexity and cost.

Experimental evaluations demonstrate that the MFN achieves a regression precision of 4.84 ± 0.15 nm using 3×10^5 simulated interferograms for pretraining, and reaches a classification accuracy of 98% on real test data after fine-tuning with only 0.24% of the pretraining dataset (approximately 5×10^2 real interferograms). Under severe mixed-noise conditions, the proposed model maintains stable displacement accuracy of about 16 nm, whereas the conventional Heuristic Analytical Algorithm (HAA) exhibits fitting errors exceeding 100 nm. Moreover, the MFN completes inference in approximately 10 ms per image—over four orders of magnitude faster than HAA, which typically requires hundreds of seconds per frame. These results confirm that the proposed framework effectively combines precision, robustness, and computational efficiency, enabling scalable, real-time interferometric metrology for both research and industrial applications.

Overall, the MFN offers a data-driven, hardware-efficient, and noise-tolerant solution for nanoscale displacement sensing. Meanwhile, current performance is mainly limited by the calibration accuracy of the voltage–displacement (V–d) measurement device, which mainly influences the accuracy of displacement head when finetuning (Detailed error and accuracy analysis can be found in the supplementary document.). Future work will improve in system calibration, particularly in voltage–displacement (V–d) precision, and focus on extending this architecture to other forms of phase-related measurement, such as angular, thermal, and material property sensing.

Code availability. The scripts for defining, training, and evaluating our MFN model, as well as the scripts for generating simulated datasets, are all stored in [MFN-for-Micro-displacement-Measurement](#).

Supplemental document. See Supplemental Document for supporting content.

References

1. B. P. Abbott, R. Abbott, T. D. Abbott, *et al.*, "Observation of gravitational waves from a binary black hole merger," *Phys. review letters* **116**, 061102 (2016).
2. C. Bond, D. Brown, A. Freise, and K. A. Strain, "Interferometer techniques for gravitational-wave detection," *Living reviews relativity* **19**, 3 (2016).
3. X. Wang, J. Su, J. Yang, *et al.*, "Modified homodyne laser interferometer based on phase modulation for simultaneously measuring displacement and angle," *Appl. Opt.* **60**, 4647–4653 (2021).
4. V. K. Chhaniwal, A. Anand, and C. S. Narayanamurthy, "Determination of refractive indices of biconvex lenses by use of a michelson interferometer," *Appl. Opt.* **45**, 3985–3990 (2006).
5. H. J. Tiziani, A. Rothe, and N. Maier, "Dual-wavelength heterodyne differential interferometer for high-precision measurements of reflective aspherical surfaces and step heights," *Appl. Opt.* **35**, 3525–3533 (1996).
6. K.-H. Chen, J.-H. Chen, S.-H. Lu, *et al.*, "Absolute distance measurement by using modified dual-wavelength heterodyne michelson interferometer," *Opt. communications* **282**, 1837–1840 (2009).
7. K. Alzahrani, D. Burton, F. Lilley, *et al.*, "Absolute distance measurement with micrometer accuracy using a michelson interferometer and the iterative synthetic wavelength principle," *Opt. Express* **20**, 5658–5682 (2012).
8. P. Psota, J. Kredba, M. Stašik, *et al.*, "Absolute wavelength scanning interferometry for measuring the thickness of optical elements," *Opt. Express* **31**, 3565–3578 (2023).
9. V. Lédl, P. Psota, F. Kaván, *et al.*, "Surface topography measurement by frequency sweeping digital holography," *Appl. Opt.* **56**, 7808–7814 (2017).
10. J. Kredba, P. Psota, M. Stašik, *et al.*, "Absolute interferometry for fast and precise radius measurement," *Opt. Express* **29**, 12531–12542 (2021).
11. K. Hornik, M. Stinchcombe, and H. White, "Multilayer feedforward networks are universal approximators," *Neural Networks* **2**, 359–366 (1989).
12. Z. Zhao, B. Li, J. Lu, *et al.*, "One-shot phase retrieval method for interferometry using a hypercolumns convolutional neural network," *Opt. Express* **29**, 16406–16421 (2021).
13. H. Yu, D. Zheng, J. Fu, *et al.*, "Deep learning-based fringe modulation-enhancing method for accurate fringe projection profilometry," *Opt. Express* **28**, 21692–21703 (2020).
14. J. Qian, S. Feng, Y. Li, *et al.*, "Single-shot absolute 3d shape measurement with deep-learning-based color fringe projection profilometry," *Opt. Lett.* **45**, 1842–1845 (2020).
15. M. Shen, L. He, H. Zhang, *et al.*, "Deep learning based measurement accuracy improvement of high dynamic range objects in fringe projection profilometry," *Opt. Express* **32**, 35689–35702 (2024).
16. R. Storn and K. Price, "Differential evolution—a simple and efficient heuristic for global optimization over continuous spaces," *J. global optimization* **11**, 341–359 (1997).
17. W. Yao, S. Azadnejad, B. Huang, *et al.*, "A deep learning approach for spatio-temporal forecasting of insar ground deformation in eastern ireland," (2025).
18. T. Huang, R. Li, Y. Zhang, *et al.*, "Diameter measurement of silicon sphere at nanometer level with laser interferometry in measurement of gravitational constant," *Measurement* **253**, 117394 (2025).
19. I. M. Sobol, "Distribution of points in a cube and approximate evaluation of integrals," *USSR Comput. mathematics mathematical physics* **7**, 86–112 (1967).
20. C. Zhu, R. H. Byrd, P. Lu, and J. Nocedal, "Algorithm 778: L-bfgs-b: Fortran subroutines for large-scale bound-constrained optimization," *ACM Trans. on mathematical software (TOMS)* **23**, 550–560 (1997).
21. S. G. Nash, "A survey of truncated-newton methods," *J. computational applied mathematics* **124**, 45–59 (2000).
22. D. Kraft, "A software package for sequential quadratic programming," *Forschungsbericht- Deutsche Forschungs- und Versuchsanstalt für Luft- und Raumfahrt* (1988).
23. K. Simonyan and A. Zisserman, "Two-stream convolutional networks for action recognition in videos," (2014).
24. J. Lee-Thorp, J. Ainslie, I. Eckstein, and S. Ontanon, "Fnet: Mixing tokens with fourier transforms," (2022).
25. S. Mehta and M. Rastegari, "Mobilevit: Light-weight, general-purpose, and mobile-friendly vision transformer," (2022).
26. Y. Gao, S. Ventura-Diaz, X. Wang, and *et al.*, "An explainable longitudinal multi-modal fusion model for predicting neoadjuvant therapy response in women with breast cancer," *Nat Commun* **15**, 9613 (2024).
27. S. Hochreiter and J. Schmidhuber, "Long short-term memory," *Neural Comput.* **9**, 1735–1780 (1997).
28. A. Maheriya, S. Panchal, A. Raval, and K. Borisagar, "Disentangled attention based multi-task learning with structural estimations for audio feature processing and identification," (2025).
29. Z. Cui, G.-J. Qi, L. Gu, *et al.*, "Multitask aet with orthogonal tangent regularity for dark object detection," (2022).
30. C. Phunruangsakao, D. Achancaray, S. I. Izumi, and M. Hayashibe, "Multibranch convolutional neural network with contrastive representation learning for decoding same limb motor imagery tasks." *Front Hum Neurosci* **16**, 1032724 (2022).
31. Y. LeCun, Y. Bengio, and G. Hinton, "Deep learning," *Nature* **521**, 436–444 (2015).
32. H. Zhao, O. Gallo, I. Frosio, and J. Kautz, "Loss functions for neural networks for image processing," (2018).
33. D. P. Kingma and J. Ba, "Adam: A method for stochastic optimization," (2017).
34. W. A. Merzouk, B. Cagneau, F. Gardillou, *et al.*, "Highly compact and easy-to-use optical chip interferometer with picometric performances," *Rev. Sci. Instruments* **87**, 103103 (2016). [_eprint: https://pubs.aip.org/aip/rsi/article-pdf/doi/10.1063/1.4963899/14053951/103103_1_online.pdf](https://pubs.aip.org/aip/rsi/article-pdf/doi/10.1063/1.4963899/14053951/103103_1_online.pdf).

35. A. Babu, T. Zhou, S. Kandel *et al.*, “Deep learning at the edge enables real-time streaming ptychographic imaging,” *Nat Commun* **14**, 7059 (2023).